Supplementary Information for Nanoscale Electric Field Imaging with an Ambient Scanning Quantum Sensor Microscope

Ziwei Qiu,[1, 2, *] Assaf Hamo,[1, †] Uri Vool,[1, 3, ‡] Tony X. Zhou,[1, 2, §] and Amir Yacoby[1, 2, ¶]

[1]*Department of Physics, Harvard University, Cambridge, MA 02138, USA*
[2]*John A. Paulson School of Engineering and Applied Sciences, Harvard University, Cambridge, MA 02138, USA*
[3]*John Harvard Distinguished Science Fellows Program, Harvard University, Cambridge MA 02138, USA*

CONTENTS

I. NV ELECTROMETRY UNDER A PERPENDICULAR MAGNETIC FIELD

A. Electron spin eigenstates

Under a bias magnetic field that is perpendicular to the NV axis, the NV electron spin ground state Hamiltonian is $H_e = D_{gs}S_z^2 + \gamma_B(B_xS_x + B_yS_y)$, where $D_{gs} \approx 2.87$ GHz is the zero-field splitting (ZFS) and $\gamma_B = 2.8$ MHz/G is the electron spin gyromagnetic ratio. The eigenstates, represented by $|0,\pm\rangle$, are superpositions of $|m_S = 0, \pm1\rangle$: $|0\rangle \approx |m_S = 0\rangle$, $|\pm\rangle \approx \frac{1}{\sqrt{2}}(|m_S = 1\rangle + e^{2i\phi_B}|m_S = -1\rangle)$[1]. As depicted in Figure 1d of the main text, the energy levels of $|\pm\rangle$ are sensitive to electric field perturbations in the XY plane $E_\perp$, with a coupling strength $d_\perp = (0.17 \pm 0.03)$ MHz/V/μm (Figure 1). Coupling to the electric field along the NV axis E_z is negligible, where the coupling strength is $d_\parallel = (3.5 \pm 0.2) \times 10^{-3}$ MHz/V/μm, so it is ignored in our analysis. We also ignore the strain in the diamond.

B. ^{15}NV vs. ^{14}NV

We choose to work with ^{15}NV in our experiments. ^{15}N has nuclear spin $I = 1/2$. The hyperfine interaction between the nuclear spin and electron spin is highly sensitive to the magnetic field angle, giving rise to electron spin echo envelope modulation (ESEEM). The magnetic field angle is carefully calibrated such that the electron spin coherence is maximized [2].

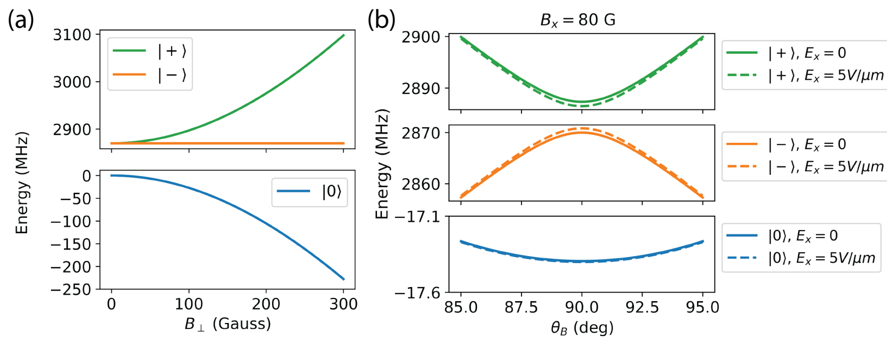

FIG. 1. The electron eigenstates $|0,\pm\rangle$ under a perpendicular magnetic field. (a) Eigenstate energy levels as a function of the perpendicular field magnitude. (b) Stark shifts induced by electric fields. Both the magnetic and electric fields are assumed to be along $\hat{x}$ in producing the plot. The coordinate system is the same as defined in Figure 1b of the main text.

The different nuclear spins carried by ^{15}N and ^{14}N cause subtle and important differences in implementing electric field sensing, as summarized in Table I. For ^{15}N, nuclear spin is $I = 1/2$, and the hyperfine coupling constant is $A_{||}$=3.65 MHz, $A_\perp$=3.03 MHz. For ^{14}N, nuclear spin is $I = 1$, and the hyperfine coupling constant is $A_{||} = A_\perp$=2.2 MHz [3, 4]. Both require a (nearly) perpendicular bias magnetic field for electric field sensing. The full NV Hamiltonian is $H = D_{gs}S_z^2 + \gamma_B \mathbf{B}\cdot\mathbf{S} + \mathbf{I}\cdot\mathbf{A}\cdot\mathbf{S} + \gamma_N \mathbf{B}\cdot\mathbf{I} + d_{||}E_z S_z^2 + d_\perp E_x(S_y^2 - S_x^2) + d_\perp E_y(S_xS_y + S_yS_x)$. ^{14}NV has an additional term due to the quadrupole interaction, QI_z^2, where $Q \approx$-5.01 MHz. Under a perpendicular magnetic field, the energy splitting between $|+\rangle$ and $|-\rangle$ is roughly $\gamma_B^2 B_\perp^2/D_{gs}$. We discuss two magnetic field regimes.

TABLE I. ^{14}NV electrometry vs. ^{15}NV electrometry

B Field	^{14}NV (I=1)	^{15}NV (I=1/2)
Weak B	only one out of three m_I states is sensitive to electric field	only one out of two m_I states is sensitive to electric field
Strong B	driving efficiency is nuclear spin dependent	both nuclear spin states contribute to signal and driving efficiency is nuclear spin independent

When $\gamma_B^2 B_\perp^2/D_{gs} < A_{\perp,||}$, i.e. $B_\perp < 33$ G, the hyperfine splitting is greater than the $|\pm\rangle$ splitting. At $\theta_B = 90°$, where θ_B is the angle between $\mathbf{B}$ and NV axis, only the $m_I = 0$ state is sensitive to magnetic field, as shown in Figure 2a. Intuitively, for $m_I \neq 0$ states, the nuclear spin exerts a hyperfine field at the electron spin, so the total magnetic field seen by the electron spin is no longer perpendicular to the NV axis. The external bias magnetic field needs to be slightly off from $\theta_B = 90°$ in order for the $m_I \neq 0$ states to be electric field sensitive, as shown in Figure 2a for ^{14}NV and Figure 2(b) for ^{15}NV. For electric field sensing to work in this weak magnetic field regime, the NV dephasing time T_2^* needs to be sufficiently long to resolve the nuclear spin sublevels. In addition, the NV fluoresence contrast, hence the signal-to-noise ratio, is reduced by $\frac{2}{3}$ for ^{14}NV and $\frac{1}{2}$ for ^{15}NV.

When $\gamma_B^2 B_\perp^2/D_{gs} > A_{\perp,||}$, i.e. $B_\perp > 33$ G, the $|\pm\rangle$ splitting is greater than the hyperfine splitting, and all the m_I states are sensitive electric field. This is because the hyperfine field that the nuclear spin exerts on the electron spin is much smaller than the external bias field, $\theta_B \approx 90°$ holds for all nuclear spin states. As shown in Figure 2c and d, a 5 $V/\mu m$ electric field causes energy shifts on all the nuclear spin states.

However, in the strong B regime, there is another subtle difference between ^{15}NV and ^{14}NV due to microwave (MW) driving. The MW field component parallel (perpendicular) to the bias magnetic field efficiently drives the transition between $|0\rangle$ and $|+\rangle$ ($|-\rangle$). Normally, MW field drives the transition between electron states while the nuclear spin state remains unchanged. However under a nearly perpendicular magnetic field, the nuclear spin state becomes electron spin dependent [2]. Transitions between all pairs of states can become allowed to some degree, and the transition amplitude is highly angle dependent and nuclear spin dependent. For example, between $|0\rangle$ and $|+\rangle$ in ^{14}NV, there are in total $3 \times 3 = 9$ possible transitions. Consequently, there is no well-defined π pulse duration. After applying a MW pulse, the electron spin can end up in different transversal plans in the Bloch Sphere, which results in a short T_2^* in measuring Rabi oscillation. Comparing Figure 3 and Figure 4, this problem is more severe in ^{14}NV than in ^{15}NV. As shown in Figure 4c and d, when driving transitions between $|0\rangle$ and $|+\rangle$ and $\theta_B \approx 90°$, only one transition is allowed for each nuclear spin sublevel.

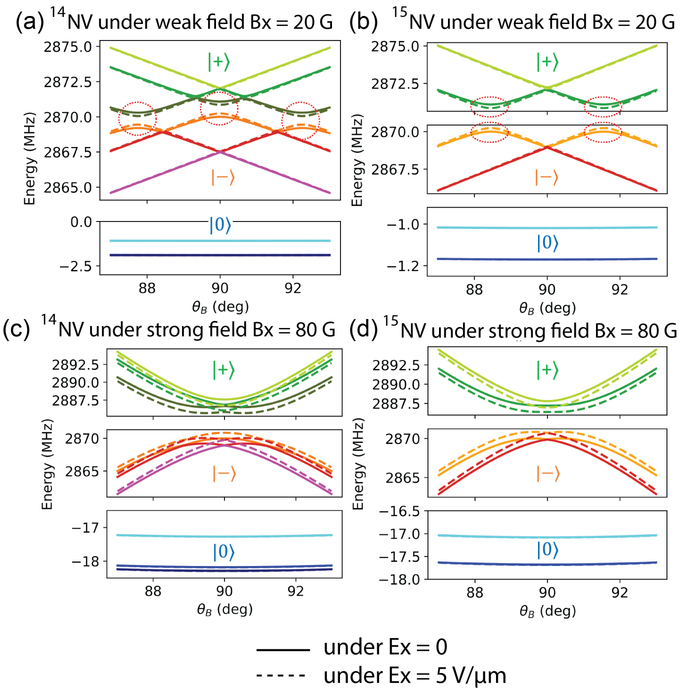

FIG. 2. Electric field sensing with ^{14}NV and ^{15}NV under different magnetic fields. (a)(b) Under a weak field, only one nuclear spin state is sensitive to electric fields. (c)(d) Under a strong field, all nuclear spin states are sensitive to electric fields.

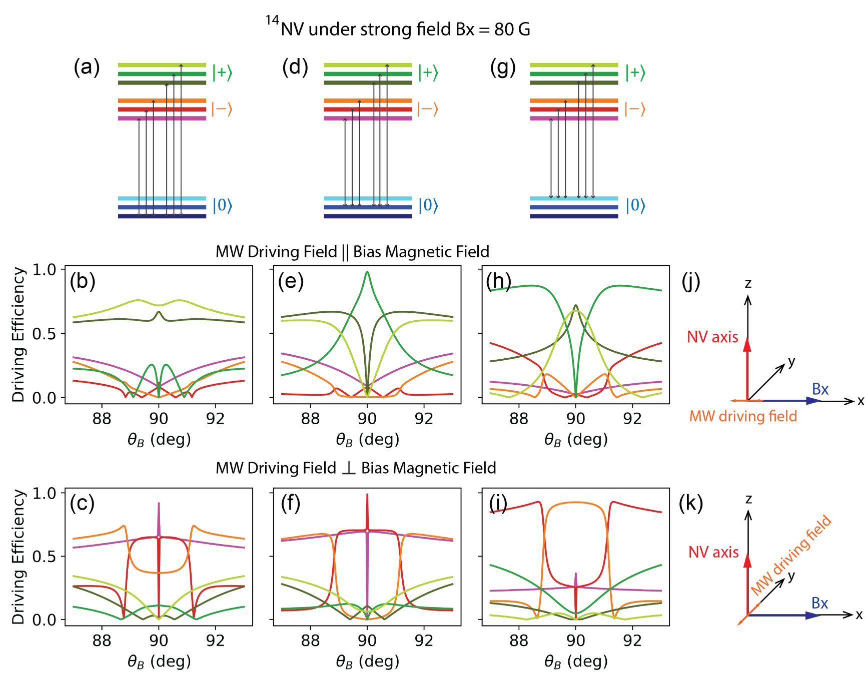

FIG. 3. Transition efficiencies of ^{14}NV under B_x=80 G. (a)(b)(c) Transition efficiencies between the lowest $|0\rangle$ nuclear sublevel and all upper levels. (b) plots the MW driving efficiency when the MW field is along the magnetic field direction, as shown in (j). (c) plots the MW driving efficiency when the MW field is perpendicular to the magnetic field direction, as shown in (k). Similarly, (d)(e)(f) and (g)(h)(i) plot the transition efficiencies between the middle and highest $|0\rangle$ nuclear sublevel and upper levels.

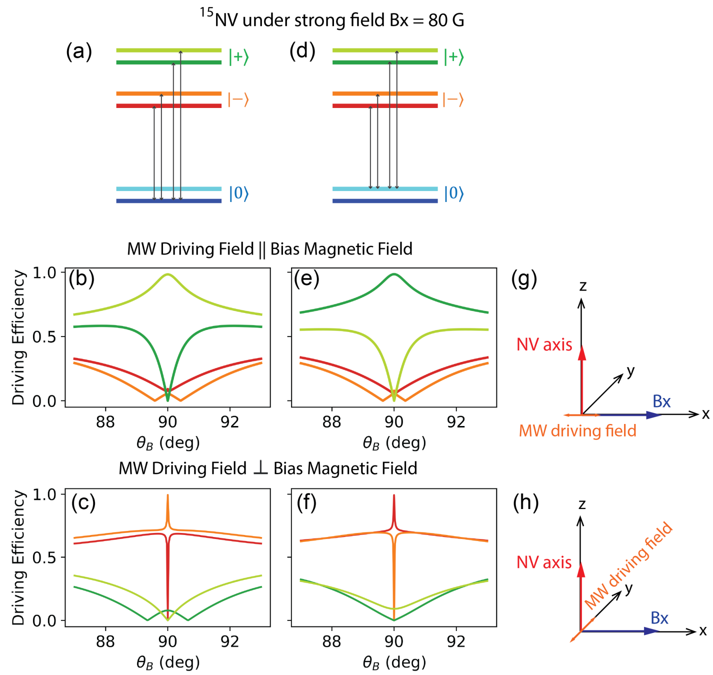

FIG. 4. Transition efficiencies of ^{15}NV under B_x=80 G. (a)(b)(c) Transition efficiencies between the lower $|0\rangle$ nuclear sublevel and all upper levels. (b) plots the MW driving efficiency when the MW field is along the magnetic field direction, as shown in (g). (c) plots the MW driving efficiency when the MW field is perpendicular to the magnetic field direction, as shown in (h). Similarly, (d)(e)(f) plots the transition efficiencies between the second $|0\rangle$ nuclear sublevel and upper levels.

II. EXPERIMENTAL DETAILS

A. Sample and NV Characteristics

The U-shaped gold structure and the RF stripline were made of Au/Ti (140nm / 12nm in thickness) by thermal evaporation on a quartz substrate. The RF stripline is about 20 μm in width.

The diamond probe was made from an electronic-grade CVD diamond, with a natural abundance (1.1%) of ^{13}C impurity spins. NV centers are created by ^{15}N ion implantation followed by vacuum annealing. They are estimated to be <40 nm deep from the surface. Details of probe fabrication can be found in [5].

We characterized the NV under a bias magnetic field ∼100 G oriented perpendicular to the NV axis. As shown in Figure 1e of the main text, due to the microwave field polarization, the $|0\rangle$-to-$|+\rangle$ transition is more efficiently driven than the $|0\rangle$-to-$|-\rangle$ transition. Figure 5a shows the Rabi oscillation between $|0\rangle$ and $|+\rangle$. Figure 5b shows the Ramsey fringes measured with a detuning of ∼1 MHz relative to the $|0\rangle \leftrightarrow |+\rangle$ transition frequency. The extracted dephasing time T_2^* is about 1.5 μs. We also measured the coherence time of the $|0\rangle$-$|+\rangle$ superposition state using spin-echo and dynamical decoupling sequences with multiple equally spaced π pulses (Figure 6)[6]. As shown in Figure 5c, T_2 increases as the number of π pulses.

Lock-in detection based on dynamical decoupling sequences was used to characterize the screening effect at high frequencies (see Figure 2c-d of the main text). Due to the finite coherence time shown in Figure 5c, measurements were performed above 200 kHz. A XY-4 sequence with $\tau = 8\,\mu$s was used in producing the data shown in Figure 3 and Figure 4 of the main text.

B. Experimental setup and control

Experiments were performed on a home-built confocal laser scanning microscope, with an AFM scanning capability [7]. The AFM contact between probe and sample is controlled by an attocube SPM controller (ASC500). Piezoelectric nanopositioners (attocube ANPxyz101 and ANPxyz100) were used for sample scanning. The quantum measurements were performed on the Quantum Orchestration Platform, a universal quantum control platform developed by Quantum

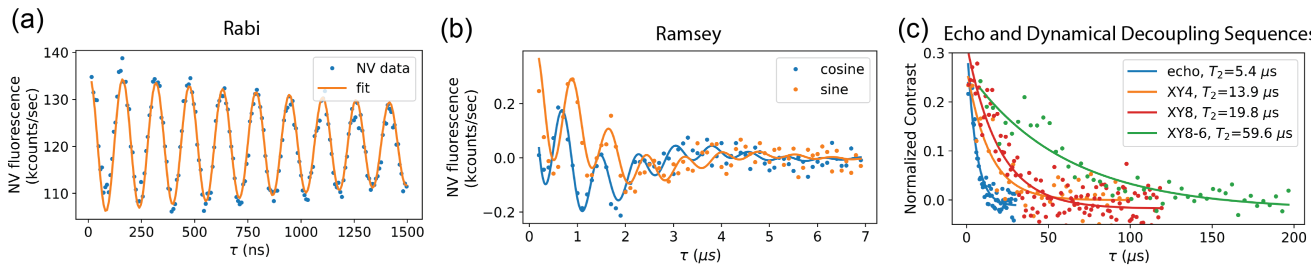

FIG. 5. Characterizations of NV coherent properties. (a) Rabi oscillation between $|0\rangle$ and $|+\rangle$. (b) Ramsey fringes measured with a detuning of $\sim$1 MHz. (c) Coherence decay measured by spin-echo and dynamical decoupling sequences.

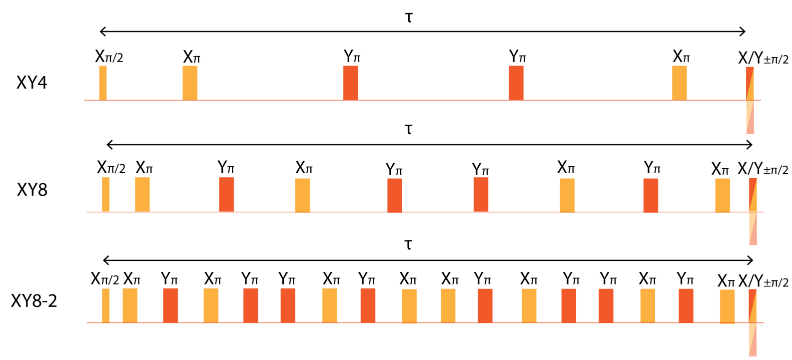

FIG. 6. Dynamical decoupling pulse sequences [6].

Machines. An Operator-X (OPX) generated control pulse sequences and measured the photon counts. Microwaves are generated by RhodeSchwartz SGS100A and amplified (Amplifier Research Model 30S1G6). NVs are optically addressed with an NA = 0.7 air objective from above, as depicted in Figure 1a of the main text. 532 nm laser of power $\sim$1 mW, pulsed by an acoustic-optical modulator (AOM), was used to initialize and readout the NV spin states. An avalanche photodiode (APD) collects the red photons from the NV fluorescence and sends the signal to the OPX.

C. Electric field sensing sequence and phase extraction

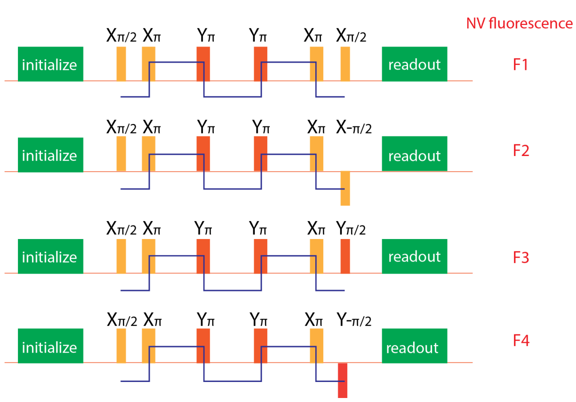

FIG. 7. AC electric field sensing sequence. The AC electric field signals, shown by the blue lines, are synchronized with the microwave pulses.

Figure 7 illustrates the XY-based AC sensing sequence used to extract the phase signal ϕ_{NV}. The AC electric field is synchronized with the MW pulse, as shown by the blue curves. The cosine and sine values of ϕ_{NV} are measured by rotating the phase of the final $\frac{\pi}{2}$ pulse:

$$\cos\phi_{NV} = 2\cdot\frac{F_2 - F_1}{F_2 + F_1}, \tag{1}$$

$$\sin\phi_{NV} = 2\cdot\frac{F_4 - F_3}{F_4 + F_3}, \tag{2}$$

where F_1, F_2, F_3 and F_4 are the NV fluorescence rates measured by the green laser pulse at the end the four sequences in Figure 7, respectively.

D. Electric field sensitivity

We first analyze the AC electric field sensitivity η_E detected by the sequence as shown in Figure 3a of the main text. The sensitivity is determined by the NV fluorescence count rate F (unit: counts per second), the optical contrast C between the states $|0\rangle$ and $|+\rangle$, the total phase accumulation time τ, the APD readout window T_r, initialization time t_{ini} as well as the electric field coupling strength $d_\perp$.

Under an electric field E_ζ, we expect NV phase accumulation $\phi_{NV} = 2\pi d_\perp E_\zeta \tau$ (the initial 2π is to convert the angle unit to rad). After a $\frac{\pi}{2}$ pulse, this phase signal is converted to the probability of being in the $|0\rangle$ state, denoted by P. With an initial $(\frac{\pi}{2})_x$ pulse and a $(\frac{\pi}{2})_y$ pulse at the end,

$$P = \frac{1}{2}(1 - \sin(\phi_{NV})) = \frac{1}{2}(1 - \sin(2\pi d_\perp E_\zeta \tau)), \tag{3}$$

Suppose a small electric field δE along $\hat{\zeta}$, the total number of photons collected due to δE after N_{avg} number of averages is:

$$\text{signal} = \left(\frac{\partial P}{\partial E}\right)_{E=0} \cdot \delta E \cdot C \cdot FT_r \cdot N_{avg} = \pi d_\perp \tau \cdot \delta E \cdot C \cdot FT_r \cdot N_{avg}, \tag{4}$$

The photon shot noise is

$$\text{noise} = \sqrt{FT_r \cdot N_{avg}} \tag{5}$$

Within 1 second of integration time, $N_{avg} = 1/(t_{ini} + \tau)$. Thus we obtain the signal-to-noise ratio (SNR) within 1 sec integration time:

$$\text{SNR} = \pi d_\perp \tau \cdot \delta E \cdot C \cdot \sqrt{\frac{FT_r}{t_{ini} + \tau}}, \tag{6}$$

The sensitivity η_E is defined as the minimal δE that can be detected with SNR = 1 within 1 sec, hence

$$\eta_E = \sqrt{\frac{t_{ini} + \tau}{FT_r}} \frac{1}{\pi d_\perp \tau C} \tag{7}$$

In AC electric field imaging, we have $F = 100$ kcounts/sec, $\tau = 8\,\mu$s, $C \approx 0.2$, $T_r = 200$ ns, and t_{ini}=2 μs. Plugging these experimental parameters and $d_\perp = 0.17$ MHz/V/μm into Equation (5), we obtain: $\eta_E = 26$ mV/μm/$\sqrt{\text{Hz}}$ = 260 V/cm/$\sqrt{\text{Hz}}$, which is comparable to the sensitivity obtained by a single NV in bulk diamonds [1].

In our motion-enabled DC electric field imaging, the directly measured signal is dominated by the local spatial gradient, so we examine the electric field gradient sensitivity: $\eta_{gradient} = \frac{\eta_E}{A}$, where A is the tip oscillation amplitude. In our experiments, $A = 13$ nm, therefore $\eta_{gradient} = 2000$ mV/μm^2/$\sqrt{\text{Hz}}$ = 2 V/μm^2/$\sqrt{\text{Hz}}$.

E. Multiple-pillar diamond probe and scanning details

Fabrication of the diamond probe follows the procedure descried in [5]. To improve the probability of finding good single NVs in a probe and scanning stability, we fabricated multiple pillars on a single probe as shown in Figure 8 and Figure 9. There are 7 pillars in a row. The outer two pillars have a diameter of ∼800 nm, and the middle five ones are 300 nm in diameter. During the scanning experiments, the probe is slightly tilted such that one of the outer thick pillar is in direct contact with the substrate which performs AFM scanning, and one of the middle thin pillar hovers above the sample of interest at a distance of 20-40 nm which performs the sensing task. The tilting angle θ_B is controlled by a manual goniometer (Edmund). This method also prevents the sensing pillar from picking up dirt or scratching the sample, and the thick AFM scanning pillar is less likely to break during harsh long-hour scanning. Overall, this multi-pillar scanning method improves the lifetime of a diamond probe.

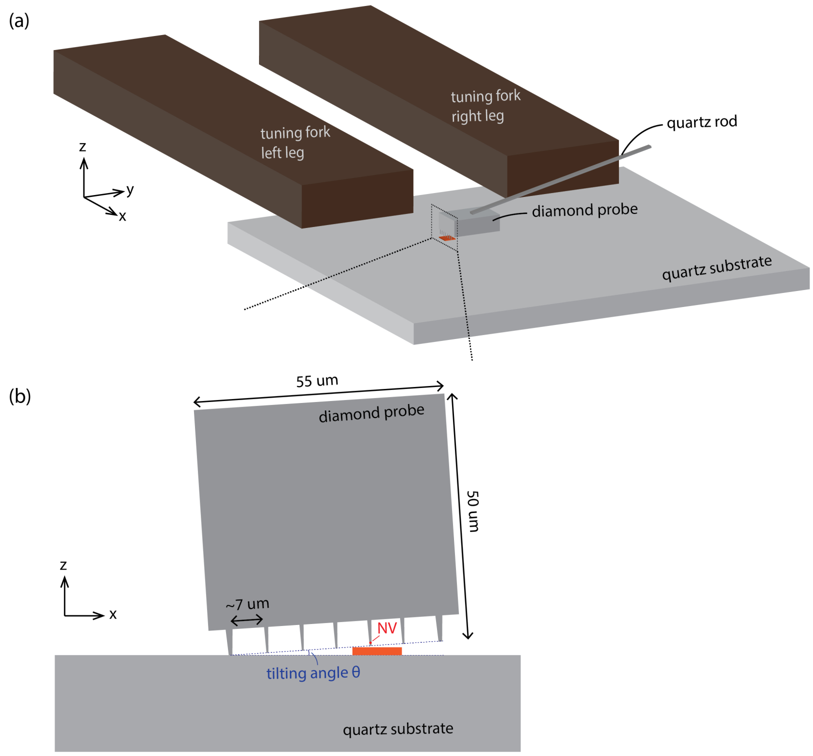

FIG. 8. (a) The probe is glued to the right leg of the tuning using a quartz rod. (b) Side view of the probe with multiple pillars. The outer two pillars are ∼800 nm in diameter. One of them is in direct contact with the substrate and performs AFM scanning. The middle five pillars are 300 nm in diameter. One of them is close to the sample of interest and performs NV quantum sensing. The NV-sample distance is hence controlled by the tilting angle θ, which is calibrated carefully.

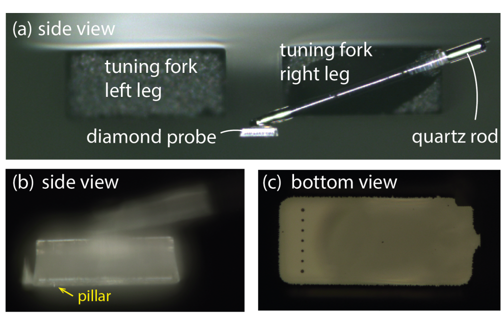

FIG. 9. Optical microscope images of the tuning fork and the diamond probe.

The tilting angle θ is carefully calibrated in advance. We start with a large θ and perform a 1D scan over two metal gaps to measure the signal profile. Based on the spatial resolution and signal strength, we gradually decrease θ, and repeats the 1D scan along the same line. As shown in Figure 3c of the main text, this process is then repeated multiple times until the signal profile is consistent with simulated signal at a distance of <100 nm away by COMSOL. More details on COMSOL simulation is included in section III.

F. Motion-enabled DC imaging

As mentioned in the main text, we observed a strong electric screening effect at DC and low frequencies. Figure 10 shows the pulsed-ESR spectra measured in the presence of DC voltages applied across the 500 nm gap. No discernible shifts were observed.

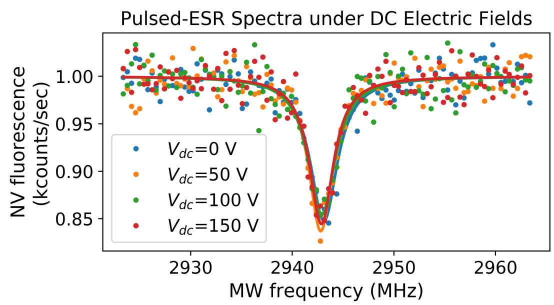

FIG. 10. Pulsed-ESR spectra showing no discernible shifts upon applying DC voltages

To overcome the electric screening effect at low frequencies, we mechanically oscillate our diamond probe in imaging DC electric field signals. The probe is attached to one of the legs of a quartz tuning fork (Figure 8 and Figure 9), and a resonant electric signal excites the motion of the tuning fork (Digi-Key 1123-ND) due to the piezoelectric properties of quartz. The fundamental mode of the tuning fork is about 32 kHz, and its clang mode is about 190 kHz, roughly 6 times higher than the fundamental (Figure 11). As shown in Figure 2 of the main text, the electric screening effect is still severe at 32 kHz, but significantly reduced at about 190 kHz, hence we excite the tuning fork at its clang mode.

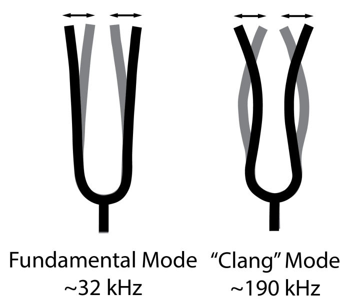

FIG. 11. Two modes of a tuning fork. The fundamental mode is used in AC imaging, and the 'clang' mode is used in DC imaging.

The probe motion increases as the excitation V_{pp}. However, the quantitative relationship varies between different tuning forks and needs to be calibrated every time when we switch a probe. In our experiments, the maximum probe motion amplitude is <20 nm, as estimated by comparing the detected signal distribution with COMSOL simulation.

III. COMSOL SIMULATION

The finite-element calculation package COMSOL performs the electrostatic simulations.

A. Dielectric screening

First, we considered dielectric screening due to the non-negligible relative permittivity of diamond, which is $\sim$5.7. Our diamond scanning tip has a circular flat top with a diameter of 300 nm, and the NV is located at $\sim$40 nm away from the surface. Figure 12 visualizes the simulated electric fields inside and outside the diamond. $E_{x,y}$ and E_z at the location of NV are both reduced to $\sim$41% as compared to the field magnitudes in the air. In subsequent discussions, we take into account this reduction to compare between the simulation and experimental data without explicitly mentioning this.

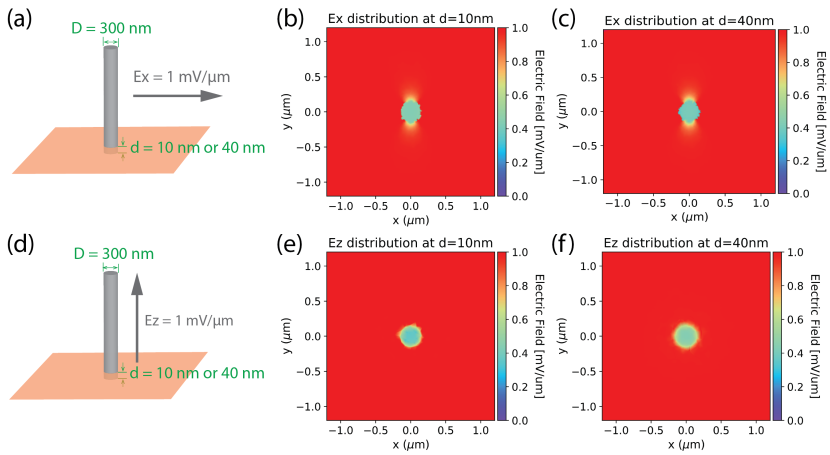

FIG. 12. COMSOL simulation of the dielectric screening effect in a diamond tip, with a flat top surface and 300 nm in diameter. (a) The probe in the presence of an external horizontal electric field of 1 $mV/\mu m$. (b) and (c) plot the 2D distribution of the simulated electric fields at depths of 10 nm and 40 nm from the tip surface respectively. (d) The external field is vertical with a magnitude of 1 $mV/\mu m$. (e) and (f) plots the simulated electric fields at depths of 10 nm and 40 nm respectively.

B. Simulation of AC and DC electric field distributions

To simulate our device, we used the real device dimension to model the geometry. In 3D simulations, The 2D lithography design was imported and extruded for a thickness of 150 nm to create 3D structures. The NV electric field sensitivity is maximized along a particular direction, which depends on the NV orientation and bias magnetic field direction. As shown in Figure 1 of the main text, the energy shift caused by electric field is $\propto E_\perp \cos(2\phi_B + \phi_E)$, so the direction of maximum sensitivity is at $\phi_E = -2\phi_B$, represented by $\hat{\zeta}$. In COMSOL simulation, we first calculated the 2D distribution of all the three components of electric fields E_x, E_y and E_z at different distances h from the sample surface in the air, then calculated the $\hat{\zeta}$ component: $E_{\hat{\zeta}} = (E_x \cos\phi + E_y \sin\phi)\sin\theta + E_z \cos\theta$, where ϕ is the azimuth angle and θ is the zenith angle as depicted in Figure 13.

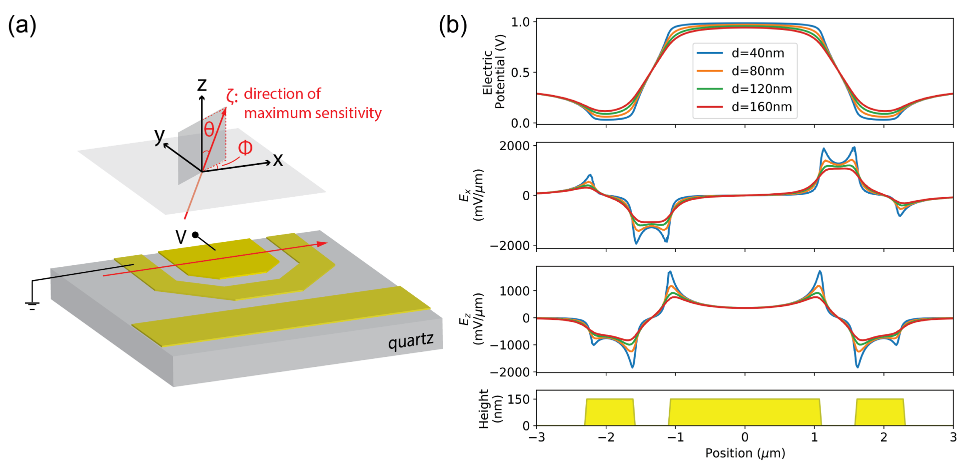

FIG. 13. COMSOL simulation of the electric potential and electric field profiles along a 1D line, represented by a red arrow in (a). The first three plots in (b) show the simulated profiles at several distances, and the fourth plot shows the metal height profile. The actual electric field detected by the NV is the component along ζ, which is a linear combination of E_x and E_z.

In imaging AC electric fields, the signal is modulated at ~250 kHz. In imaging DC electric fields, both the probe and signal oscillate at $\sim$ 190 kHz. ϕ, θ and the distance h are the three free parameters to produce Figure 3e of the main text, where we used $\phi = 20°, \theta = 45°, h = 90$ nm. In DC imaging, a XY4-based AC sensing pulse sequence is synchronized with the motion of the diamond probe. Therefore, the coherent phase accumulation is proportional to the product of the electric field gradient along the probe oscillation direction and the oscillation amplitude. These are two additional free parameters in producing Figure 4e of the main text, the oscillation direction is set to be at 30° relative to the scanning direction $\hat{x}$ and the oscillation amplitude is 13 nm.

* ziweiqiu29@gmail.com
† Present address: Department of Physics, Bar-Ilan University, Ramat Gan, Israel
‡ Present address: Max Planck Institute for Chemical Physics of Solids, Dresden, Germany
§ Present address: Research Laboratory of Electronics, Massachusetts Institute of Technology, Cambridge, MA, USA
¶ Correspondence to: yacoby@physics.harvard.edu
[1] F. Dolde, H. Fedder, M. W. Doherty, T. Nöbauer, F. Rempp, G. Balasubramanian, T. Wolf, F. Reinhard, L. C. Hollenberg, F. Jelezko, *et al.*, Electric-field sensing using single diamond spins, Nature Physics **7**, 459 (2011).
[2] Z. Qiu, U. Vool, A. Hamo, and A. Yacoby, Nuclear spin assisted magnetic field angle sensing, npj Quantum Information **7**, 1 (2021).
[3] A. Gali, M. Fyta, and E. Kaxiras, Ab initio supercell calculations on nitrogen-vacancy center in diamond: Electronic structure and hyperfine tensors, Physical Review B **77**, 155206 (2008).
[4] S. Felton, A. Edmonds, M. Newton, P. Martineau, D. Fisher, D. Twitchen, and J. Baker, Hyperfine interaction in the ground state of the negatively charged nitrogen vacancy center in diamond, Physical Review B **79**, 075203 (2009).
[5] T. X. Zhou, R. J. Stöhr, and A. Yacoby, Scanning diamond nv center probes compatible with conventional afm technology, Applied Physics Letters **111**, 163106 (2017).
[6] A. M. Souza, G. A. Álvarez, and D. Suter, Robust dynamical decoupling, Philosophical Transactions of the Royal Society A: Mathematical, Physical and Engineering Sciences **370**, 4748 (2012).
[7] P. Maletinsky, S. Hong, M. S. Grinolds, B. Hausmann, M. D. Lukin, R. L. Walsworth, M. Loncar, and A. Yacoby, A robust scanning diamond sensor for nanoscale imaging with single nitrogen-vacancy centres, Nature nanotechnology **7**, 320 (2012).